Commun Nonlinear Sci Numer Simulat 133 (2024) 107956

Contents lists available at ScienceDirect

Communications in Nonlinear Science and Numerical Simulation

journal homepage: www.elsevier.com/locate/cnsns

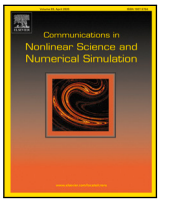

Research paper

Shape transformation on curved surfaces using a phase-field model

Hyundong Kim [a], Seungyoon Kang [b], Gyeonggyu Lee [b], Sungha Yoon [c], Junseok Kim [b,*]

[a] Department of Mathematics and Physics, Gangneung-Wonju National University, Gangneung 25457, Republic of Korea
[b] Department of Mathematics, Korea University, Seoul 02841, Republic of Korea
[c] Institute of Mathematical Sciences, Ewha Womans University, Seoul 03760, Republic of Korea

ARTICLE INFO

Keywords:
Shape transformation
Phase-field model
Curved surfaces
Stable time-stepping scheme

ABSTRACT

Shape transformation on evolving curved surfaces is essential for its diverse applications across various scientific disciplines and facilitates the deeper understanding of natural phenomena, the development of new materials, and engineering design optimization. In this study, we develop a phase-field model and its numerical methods for shape transformation on curved surfaces. A modified surface Allen–Cahn (AC) equation with a fidelity term is proposed to simulate shape transformation on curved surfaces. To numerically solve the modified surface AC equation on curved surfaces, we propose a fully explicit scheme and an unconditionally stable method. The proposed stable approach is not only simple and efficient to implement numerically but is also unconditionally stable and eliminates the restrictive temporal time step size constraints. Through numerical experiments using the proposed approach, we demonstrate that shape transformation on evolving curved surfaces can be implemented on both simple and complex curved surfaces.

1. Introduction

Shape transformation is a process that constructs a sequence of shapes between the source and target, which is widely applied in various fields such as medicine, remote sensing, graphics, and special effects creation among others. For instance, it is applied to visualize the transition between chimpanzee and human braincases using mesh parametrization [1]. Using the above-mentioned method, the authors demonstrated how mesh parametrization and shape transformation can be combined to obtain a consistent quantitative description. In [2], the Navier–Stokes equation and a front-tracking method were used for three-dimensional (3D) shape transformation to simulate vesicle dynamics. Vesicle deformation plays a role in trembling, vacillation-breathing, and swinging motions, which are new types of unsteady motion. Recently, shape and function transformation approaches were researched on polymeric film surfaces to use special shapes for the physical function of materials, which depend on their shape or dimension [3]. The phenomenon of temperature-driven reversible shape transformation of thermo-responsive particles in block copolymer domains has been studied [4]. The authors found the shape transformation phenomenon in block copolymer particle shape: transition between onion-like (stripes) shape and raspberry-like (spots) shape particles under different specific temperature conditions. It is important to derive desired results through experiments; however, it is complex and difficult to implement while satisfying the desired conditions. Furthermore, it consumes a significant amount of time and cost. One solution to these issues is to implement the process in numerical simulation. In this work, we shall numerically simulate shape transformation on curved surfaces using a phase-field model.

Meanwhile, a shape transformation using a phase-field model [5,6] has been researched to reconstruct 3D volumes from multi-slice data. When reconstructing a 3D volume from multiple slice data, accurate and smooth volume reconstruction is difficult

* Corresponding author.
E-mail addresses: hdkim@gwnu.ac.kr (H. Kim), cfdkim@korea.ac.kr (J. Kim).
URL: https://mathematicians.korea.ac.kr/cfdkim/ (J. Kim).

https://doi.org/10.1016/j.cnsns.2024.107956
Received 2 November 2023; Received in revised form 16 February 2024; Accepted 5 March 2024
Available online 11 March 2024

if information between slices are insufficient. To overcome these technical difficulties, shape transformation using a phase-field model is applied between a slice (source) and another slice (target). During this process, the necessary intermediate data can be found and stacked while shape transforming between the source slice and the target slice. Then, the 3D is reconstructed using the stacked data. Here, to perform the shape transformation, the modified Allen–Cahn (AC) equation with fidelity term is used. The AC equation [7,8] is a phase-field model that includes a diffusion term which has property as the total energy decreasing, motion by mean curvature flows. The modified AC equation with other terms can be served by various tasks, representatively, such as 3D volume reconstruction [9], image inpainting [10], processing [11], smoothing [12], topology optimization [13], and segmentation [14]. The modified AC equation with Chan–Vese fitting term is studied numerically by an unconditionally stable hybrid scheme in [14]. The authors presented image segmentation using the proposed algorithm. The conservative AC equation which includes a Lagrange multiplier is studied in [15]. The authors described numerical scheme to solve the AC type equations on surfaces. Their proposed scheme has a second order convergence rate in time and space, is unconditionally stable, and can implement motion by mean curvature by numerical simulations. To numerically study the surface AC type equations, the explicit hybrid numerical method [16] was developed by using the operator splitting method and the discrete Laplace–Beltrami operator on triangulated surfaces. In the numerical tests, the authors demonstrate the efficiency and accuracy of the proposed method using the motion by mean curvature property.

The related previous works [17,18] have studied the shape transformation using the modified AC equation with a fidelity term in two- or three-dimensional spaces. The basic mechanism of the modified AC equation with fidelity term for the shape transformation is as follows: first, the AC equation maintains the transition layer of the interface between phases as a hyperbolic tangent profile; second, the fidelity term transforms the shape from the source to the target. The advantage of the modified AC equation lies in its ability to allow smooth and natural shape transformations. For a more detailed explanation, please refer to the reference paper [17]. If shape transformation is performed in the 3D space, it requires a lot of computational cost and time. Although the explicit type scheme has the advantage of being simple to implement, it is difficult to use a time step value as large as desired because there is a strict time step constraint when numerically solving the diffusion equation part. To resolve these shortcomings, a numerical method has been studied that uses the alternating direction explicit (ADE) finite difference method (FDM) [19] to relax the time step constraint. This algorithm is stable when numerically solving the diffusion equation part [20] and allows fast shape transformation in the 3D space using a relatively large value of the time step value [21].

In this work, we will develop shape transformation on curved surfaces using the modified surface AC equation. Therefore, to simply solve the modified surface AC equation on the curved surface domain, we use the operator splitting method and explicit time-stepping scheme [22,23], which is based on a discretization of Laplace–Beltrami operator [24–26]. Then, we conduct numerical simulations to investigate shape transformations on curved surfaces. The standard Laplace operator cannot be directly applied on curved surface domain when using the explicit type numerical method. To solve the diffusion equation part on curved surface domain, the Laplace–Beltrami operator is introduced to the curved surface domain. The numerical schemes to solve the discretized Laplace–Beltrami operator on curved surface were developed in [24–28]. The discretized Laplace–Beltrami operators are easily implemented numerically and have been applied in numerical simulations on curved surfaces such as pattern formation on evolving surfaces [22,23] and deformable 3D shape matching for virtual clothing trials [29]. In [29], the authors presented a method for virtual clothing in online shopping using 3D point matching and Kinect camera technology. The approach surpasses design and style constraints and shows promising results in visual evaluations.

Recently, a numerically efficient method was developed for solving the Cahn–Hilliard–Navier–Stokes system on complex surface domains. This approach, which achieves second-order accuracy and unconditional energy stability, involves the application of the Laplace–Beltrami operator, Jacobi iteration, and the bi-conjugate gradient stabilized method on curved surfaces [30]. The authors applied the proposed approach to simulate the evolution of two phases on complex curved surfaces subjected to fluid flows. In [31], the authors developed first- and second-order unconditionally stable approaches. This approach consists of the Laplace–Beltrami operator and the linearly stabilized splitting scheme. It is designed to efficiently solve the multi-component Cahn–Hilliard equations and to present multi-component phase separation on curved surface domains [32,33].

The research is structured as follows. The phase-field model and its numerical solution algorithm are introduced in Section 2. In Section 3, we conduct numerical experiments to demonstrate the performance of the proposed method for shape transformation on curved surfaces and propose the unconditionally stable scheme on curved surfaces. The discussions and conclusions are given in Sections 4 and 5, respectively.

2. Phase-field model and its numerical solution algorithms

In this section, we present a phase-field equation for shape transformation on curved surfaces and describe its numerical solution algorithms using the Laplace–Beltrami operator and the operator splitting method.

2.1. Phase-field model

Let us consider the following modified surface AC equation for shape transformation on curved surfaces [17].

$$\frac{\partial \phi(\mathbf{x},t)}{\partial t} = -\frac{F'(\phi(\mathbf{x},t))}{\epsilon^2} + \Delta_S \phi(\mathbf{x},t) + \alpha\sqrt{F(\phi(\mathbf{x},t))}(\psi(\mathbf{x}) - \phi(\mathbf{x},t)), \tag{1}$$

where $\mathcal{S}$ is a closed smooth curved surface, $\mathbf{x} \in \mathcal{S}$, $t > 0$, ϵ is a small positive constant governing the thickness of interface, α is a positive constant controlling the fidelity between the source and target shapes, $F(\phi(\mathbf{x},t)) = (\phi^2(\mathbf{x},t) - 1)^2/4$ represents a double-well

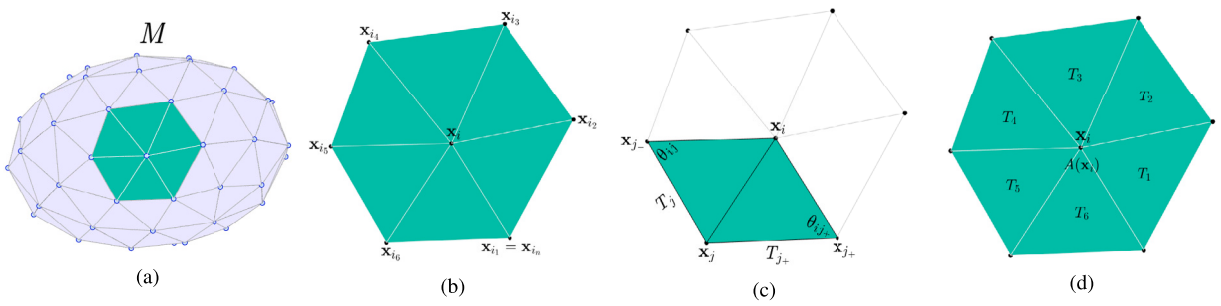

Fig. 1. Schematics of (a) triangulated surface, (b) one-ring neighbors of $\mathbf{x}_i$ with $i_1 = i_n$, (c) triangles T_j and T_{j+}, and (d) area $A(\mathbf{x}_i)$.

potential, and Δ_S denotes the Laplace–Beltrami operator. If we use the standard Laplacian Δ and set $\alpha = 0$, then the modified surface AC equation with fidelity term transforms into the classical AC equation [7], which is a mathematical model to describe the evolutionary dynamics of a non-conserved phase-field in the process of anti-phase domain coarsening of binary alloys. With $\phi(\mathbf{x}, t)$ being the phase-field, $\phi(\mathbf{x}, 0)$ is the source shape and $\psi(\mathbf{x})$ is the target shape. Because we are using the double-well potential, we basically assume that $\min_{\mathbf{x}\in S} \psi(\mathbf{x}) = -1$ and $\max_{\mathbf{x}\in S} \psi(\mathbf{x}) = 1$. However, if it is not the case, the following normalization is used to bound the target shape $\psi(\mathbf{x})$ in $[-1, 1]$.

$$\psi(\mathbf{x}) := \frac{2\psi(\mathbf{x}) - \max\limits_{\mathbf{x}\in S} \psi(\mathbf{x}) - \min\limits_{\mathbf{x}\in S} \psi(\mathbf{x})}{\max\limits_{\mathbf{x}\in S} \psi(\mathbf{x}) - \min\limits_{\mathbf{x}\in S} \psi(\mathbf{x})}.$$

Eq. (1) can be derived by taking the total energy functional derivative in L^2 [34],

$$\mathcal{E}(\phi) := \int_S \left[\frac{F(\phi)}{\epsilon^2} + \frac{1}{2}|\nabla_S \phi|^2 + \frac{\alpha}{2}\left(\left(\frac{\phi^3}{3} - \phi\right)\psi - F(\phi)\right)\right] d\mathbf{x},$$

where ∇_S is a surface gradient. Note that $\partial\phi/\partial t = -\delta\mathcal{E}/\delta\phi$, where $\delta\mathcal{E}/\delta\phi$ is the variational derivative of the total energy functional.

2.2. Numerical solution algorithms

2.2.1. Discretization

Let us consider the simple discretized Laplace–Beltrami operator [24,26] on closed smooth curved surfaces S. On the triangulated surface mesh M of the given closed smooth surface S (see, Fig. 1(a)), we define the surface vertex set $\{\mathbf{x}\}_{i=1}^N$ including N points. Let $V(i) = \{i_1, i_2, \ldots, i_m\}$ be the one-ring neighbor surface vertex indices, with $i_1 = i_m$ for a given surface vertex $\mathbf{x}_i$ (see Fig. 1(b)). The surface vertices $\mathbf{x}_i$, $\mathbf{x}_{j_-}$ and $\mathbf{x}_j$ constitute a triangle T_j. We compute $A(\mathbf{x}_i)$ in Fig. 1(d), the sum of triangles T_j in contact with the curved surface vertex $\mathbf{x}_i$ [24].

Let $A(\mathbf{x}_i, T_j)$ be the area of triangle T_j in contact with $\mathbf{x}_i$. Then, it can be expressed using $\mathbf{x}_i$, $\mathbf{x}_j$, and $\mathbf{x}_{j_-}$, three vertices of T_j, see Fig. 1(c), as follows:

$$\begin{aligned} A(\mathbf{x}_i, T_j) &= \frac{1}{2}|\mathbf{x}_j - \mathbf{x}_i||\mathbf{x}_{j_-} - \mathbf{x}_i| \sin\theta = \frac{1}{2}|\mathbf{x}_j - \mathbf{x}_i||\mathbf{x}_{j_-} - \mathbf{x}_i|\sqrt{1 - \cos^2\theta} \\ &= \frac{1}{2}\sqrt{|\mathbf{x}_j - \mathbf{x}_i|^2|\mathbf{x}_{j_-} - \mathbf{x}_i|^2 - |\mathbf{x}_j - \mathbf{x}_i|^2|\mathbf{x}_{j_-} - \mathbf{x}_i|^2\cos^2\theta} \\ &= \frac{1}{2}\sqrt{|\mathbf{x}_j - \mathbf{x}_i|^2|\mathbf{x}_{j_-} - \mathbf{x}_i|^2 - \left(\mathbf{x}_j - \mathbf{x}_i, \mathbf{x}_{j_-} - \mathbf{x}_i\right)^2}, \end{aligned} \tag{2}$$

where θ is the angle of vertex $\mathbf{x}_i$ and $(\mathbf{a}, \mathbf{b})$ is the inner product for the vectors $\mathbf{a}$ and $\mathbf{b}$. Therefore, $A(\mathbf{x}_i)$ can be calculated as $A(\mathbf{x}_i) = \sum_{j\in V(i)} A(\mathbf{x}_i, T_j)$. Let $\phi_i = \phi(\mathbf{x}_i)$. Under curvature normal formula [26,27]

$$\lim_{A(\mathbf{x}_i)\to 0} = \frac{3\nabla A(\mathbf{x}_i)}{2A(\mathbf{x}_i)} = -H(\mathbf{x}_i), \tag{3}$$

where $H(\mathbf{x}_i)$ denotes the mean curvature normal at point $\mathbf{x}_i$ and we applied Eq. (2). Partial derivatives of $A(\mathbf{x}_i)$ respect to coordinates of $\mathbf{x}_i$ are calculated. Though it is not trivial, we derive the following discretized Laplace–Beltrami operator [25,35]:

$$\Delta_S \phi_i = \frac{3}{A(\mathbf{x}_i)} \sum_{j\in V(i)} \frac{\cot\theta_{ij} + \cot\theta_{ij_+}}{2}(\phi_j - \phi_i), \tag{4}$$

where θ_{ij} is the angle in triangle T_j and θ_{ij_+} is the angle in triangle T_{j+} as shown in Fig. 1(c). By dividing the inner product of vectors $(\mathbf{x}_{j_-} - \mathbf{x}_i, \mathbf{x}_j - \mathbf{x}_{j-})$ and $(\mathbf{x}_j - \mathbf{x}_{j+}, \mathbf{x}_{j+} - \mathbf{x}_i)$ by the their outer product, the above-mentioned cotangent formula can be simply expressed as cotangent with angles $\theta_{ij} = \angle(\mathbf{x}_{j_-} - \mathbf{x}_i, \mathbf{x}_j - \mathbf{x}_{j_-})$ and $\theta_{ij+} = \angle(\mathbf{x}_j - \mathbf{x}_{j+}, \mathbf{x}_{j+} - \mathbf{x}_i)$.

2.2.2. Numerical solution algorithm for the modified surface AC equation with fidelity term

Now, we use the operator splitting method to solve the modified surface AC Eq. (1) by decomposing it into the following three terms:

$$\frac{\partial \phi_1(\mathbf{x},t)}{\partial t} = \Delta_S \phi_1(\mathbf{x},t), \tag{5}$$

$$\frac{\partial \phi_2(\mathbf{x},t)}{\partial t} = -\frac{F(\phi_2(\mathbf{x},t))}{\epsilon^2}, \tag{6}$$

$$\frac{\partial \phi_3(\mathbf{x},t)}{\partial t} = \alpha\sqrt{F(\phi_3(\mathbf{x},t))}(\psi(\mathbf{x}) - \phi_3(\mathbf{x},t)). \tag{7}$$

Here, ϕ_1, ϕ_2, and ϕ_3 represent the solutions for the three subproblems Eqs. (5), (6), and (7), respectively. The modified surface AC Eq. (1) can be discretized in the following three steps. First, we use the explicit Euler scheme to numerically solve the diffusion Eq. (5) using a time step Δt.

$$\frac{\phi_{1,i}^{n+1} - \phi_i^n}{\Delta t} = \Delta_S \phi_i^n, \tag{8}$$

Second, we apply the separation of variables to solve the reaction term (6)

$$\phi_{2,i}^{n+1} = \frac{\phi_{1,i}^{n+1}}{\sqrt{\left(1 - \left(\phi_{1,i}^{n+1}\right)^2\right) e^{-\frac{2\Delta t}{\epsilon^2}} + \left(\phi_{1,i}^{n+1}\right)^2}}. \tag{9}$$

Finally, let us apply the semi-implicit Euler method to solve the fidelity term (7) as follows.

$$\frac{\phi_{3,i}^{n+1} - \phi_{2,i}^{n+1}}{\Delta t} = \alpha\sqrt{F\left(\phi_{2,i}^{n+1}\right)}(\psi_i - \phi_{3,i}^{n+1}),$$

which can be rewritten as

$$\phi_i^{n+1} = \phi_{3,i}^{n+1} = \frac{\phi_{2,i}^{n+1} + \Delta t\alpha\psi_i\sqrt{F\left(\phi_{2,i}^{n+1}\right)}}{1 + \Delta t\alpha\sqrt{F\left(\phi_{2,i}^{n+1}\right)}}. \tag{10}$$

Remark 1. In this study, we focused on shape transformation on curved surfaces using a phase-field model. We use the proposed operator splitting scheme (8)–(10), which is only first-order accurate in time, for simplicity of exposition. Although it may be slightly complex, we can design and analyze a second-order accurate operator splitting scheme based on the ideas from Refs. [36,37].

Remark 2. Here, we present a mathematical model, its numerical scheme and simulation results for shape transformation on curved surfaces. We analyzed the numerical stability of the proposed operator splitting numerical scheme (8)–(10). To prove the convergence analysis, we may refer to existing works [36–40] on stability and convergence analysis of operator splitting numerical schemes.

2.2.3. Stability analysis of the fully explicit scheme

Next, we consider the stability analysis for the proposed method. Let us define the discrete maximum norm as $\|\phi\|_\infty = \max_{1\le i\le N}|\phi_i|$. Let us assume $\|\phi_1^n\|_\infty \le 1$ and all triangular surface meshes are acute triangles. From Eq. (8),

$$|\phi_{1,i}^{n+1}| = \left|\left(1 - \frac{3\Delta t}{A(\mathbf{x}_i)}\sum_{j\in V(i)}\frac{\cot\theta_{ij} + \cot\theta_{ij_+}}{2}\right)\phi_i^n + \frac{3\Delta t}{A(\mathbf{x}_i)}\sum_{j\in V(i)}\frac{\cot\theta_{ij} + \cot\theta_{ij_+}}{2}\phi_j^n\right| \tag{11}$$

$$\le \left(1 - \frac{3\Delta t}{A(\mathbf{x}_i)}\sum_{j\in V(i)}\frac{\cot\theta_{ij} + \cot\theta_{ij_+}}{2}\right)\|\phi^n\|_\infty + \frac{3\Delta t}{A(\mathbf{x}_i)}\sum_{j\in V(i)}\frac{\cot\theta_{ij} + \cot\theta_{ij_+}}{2}\|\phi^n\|_\infty \tag{12}$$

$$= 1,\ i = 1,\dots,N, \tag{13}$$

where we have used $0 < \theta_{ij} < \pi/2$ and $0 < \theta_{ij_+} < \pi/2$, i.e., $\cot\theta_{ij} > 0$ and $\cot\theta_{ij_+} > 0$; and the non-negative coefficient condition as follows:

$$1 - \frac{3\Delta t}{A(\mathbf{x}_i)}\sum_{j\in V(i)}\frac{\cot\theta_{ij} + \cot\theta_{ij_+}}{2} \ge 0,\ i = 1,\dots,N, \tag{14}$$

which can be rewritten as

$$\Delta t \le \min_{1\le i\le N}\frac{2A(\mathbf{x}_i)}{3\sum_{j\in V(i)}(\cot\theta_{ij} + \cot\theta_{ij_+})}. \tag{15}$$

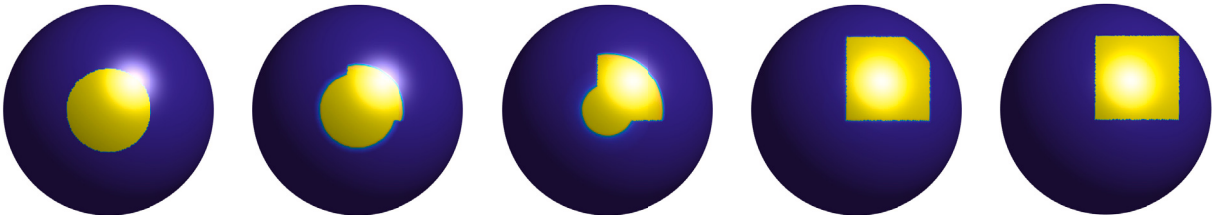

(a) Source (b) $t = 10\Delta t$ (c) $t = 30\Delta t$ (d) $t = 100\Delta t$ (e) Target

Fig. 2. (a) Circle source shape, (e) Square target shape, and (b)–(d): shape transformation from circular to square shapes.

Therefore, $\|\phi_1^{n+1}\|_\infty \le 1$ holds for Δt satisfying the time step constraint, Eq. (15). Next, from Eq. (9), we have

$$|\phi_{2,i}^{n+1}| = \frac{|\phi_{1,i}^{n+1}|}{\sqrt{\left(1-\left(\phi_{1,i}^{n+1}\right)^2\right)e^{-\frac{2\Delta t}{\epsilon^2}}+\left(\phi_{1,i}^{n+1}\right)^2}} \le 1,\ i=1,\dots,N, \tag{16}$$

where we have used $1-\left(\phi_{1,i}^{n+1}\right)^2 \ge 0$ because of $\|\phi_1^{n+1}\|_\infty \le 1$. Therefore, $\|\phi_2^{n+1}\|_\infty \le 1$ holds. Finally, from Eq. (10), we have

$$|\phi_i^{n+1}| \le \frac{|\phi_{2,i}^{n+1}| + \Delta t\alpha|\psi_i|\sqrt{F\left(\phi_{2,i}^{n+1}\right)}}{1+\Delta t\alpha\sqrt{F\left(\phi_{2,i}^{n+1}\right)}} \le 1,\ i=1,\dots,N,$$

where we have used $\|\phi_2^{n+1}\|_\infty \le 1$ and $\|\psi\|_\infty \le 1$. Hence, $\|\phi^{n+1}\|_\infty \le 1$ holds for Δt satisfying the time step constraint, Eq. (15).

3. Numerical experiments

In this section, we shall perform several numerical experiments using the proposed modified surface AC equation to simulate shape transformations on simple or complex curved surfaces.

3.1. Simple shape transformation on sphere

First, we perform the shape transformation on a static sphere. On a triangulated static sphere, the source shape $\phi(x,y,z,0)$ is set to a circle and the target shape $\psi(x,y,z)$ is set to a square, as follows:

$$\begin{aligned}\phi(x,y,z,0) &= \begin{cases} 1 & \text{if } \sqrt{x^2+y^2} < 40,\ z>0,\\ -1 & \text{otherwise.}\end{cases}\\ \psi(x,y,z) &= \begin{cases} 1 & \text{if } |x-30|-40<0,\ |y-30|-40<0,\ z>0,\\ -1 & \text{otherwise.}\end{cases}\end{aligned} \tag{17}$$

Here, we used the parameter values as $\Delta t = 0.05$, $\epsilon = 3$, and $\alpha = 10$. Fig. 2(a) and (e) show the circle source shape and square target shape on a sphere, respectively. In Fig. 2(b)–(d), we can see that the shape transformation from a circle to a square on the sphere. In the overlapping region between the circular source and square target shapes, shape transformation occurs smoothly on the spherical surface. During this process, the AC equation part preserves a smooth phase transition layer, with the fidelity term incorporating the phase-field value into the target position area and subtracting it outside the target region.

3.2. Complex shape transformation on sphere

Next, using the proposed method on a triangulated sphere, let us consider a more complex shape transformation by loading image files, such as from a larva image source into a butterfly image target. To construct the source and target shapes, we used projection plane to the given triangulated spherical surface domain. To perform this projection, we use the linear fitting. Here, we use the values of parameters as $\Delta t = 0.05$, $\lambda = 10^6$, and $\epsilon = 3$. Fig. 3(a) and (h) show the source shape as a larva image and the target shape as a butterfly image. The evolution over time first occurs in the overlapping regions of the source and target in Fig. 3(b). Next, the shape is transformed to the butterfly image target shape while preserving the smooth transition layer in Fig. 3(c) to (f). Finally, we can see in Fig. 3(g) that the butterfly's wings are fully formed and the shape transformation is successfully completed. Through this numerical experiment, we can validate that the shape transformation of complex shapes on a triangular spherical surface domain proceeds smoothly on the given curved surface by applying the proposed method.

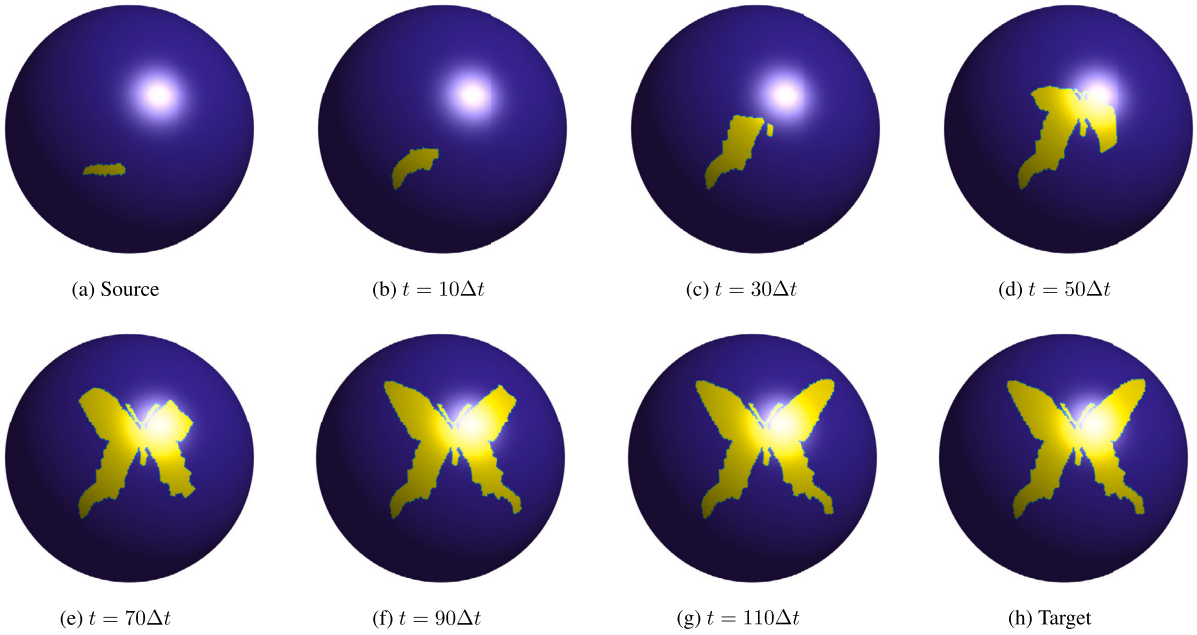

Fig. 3. (a) Larva image source shape on a triangulated sphere. (h) Butterfly image target shape on a triangulated sphere. (b)–(g): Temporal evolution of shape transformation from larva image source shape to butterfly image target shape on a triangulated sphere.

3.3. Pattern transformation on curved surfaces

In this section, on triangulated static curved surfaces and evolving curved surfaces, we perform multiple shape transformations on complex curved surface and a shape transformation for Turing patterns [22,23].

3.3.1. Multiple shape transformations on complex curved surface

Now, we shall perform multiple shape transformations on the complex curved surface representing a Stanford bunny surface. Let us consider simple shapes such as the circle, the triangle, and the rectangle. In this test, the triangle is defined as the target shape until $t = 100\Delta t$, and then is defined as the source shape thereafter. We set the source shapes to be the circle $\phi(x, y, z, 0)$ and the triangle $\psi_1(x, y, z)$, and set the target shapes to be the triangle $\phi_1(x, y, z, 100\Delta t)$ and the rectangle $\psi_2(x, y, z)$ as follows:

$$\begin{aligned}
\phi(x, y, z, 0) &= \begin{cases} 1 & \text{if } \sqrt{(x+23.06)^2 + (y+1.61)^2 + (z-4.44)^2} < 8, \\ -1 & \text{otherwise.} \end{cases} \\
\psi_1(x, y, z) = \phi_1(x, y, z, 100\Delta t) &= \begin{cases} 1 & \text{if } y > -8.69,\ y < \sqrt{3}|(x-7.70)| + 3.31,\ z > -4.00, \\ -1 & \text{otherwise.} \end{cases} \\
\psi_2(x, y, z) &= \begin{cases} 1 & \text{if } |x+6.40| - 5.6 < 0,\ |z-2.09| - 2.7 < 0,\ y > -14.50, \\ -1 & \text{otherwise.} \end{cases}
\end{aligned} \tag{18}$$

Here, we used the parameter values as $\Delta t = 0.01$, $\epsilon = 3$ and $\lambda = 10$. This numerical experiment is performed as follows. First, a shape transformation is performed from $\phi(x, y, z, 0)$ to $\psi_1(x, y, z)$, which can be seen in Fig. 4(a)–(c), and then, shape transformation is also carried out from $\phi_1(x, y, z, 100\Delta t)$ to $\psi_2(x, y, z)$, which can be seen in Fig. 4(c)–(f). Using the proposed method, we implemented multiple shape transformations on the complex curved surface. In the numerical results, it can be seen that shape transformations are smooth and well performed on the given complex curved surface.

3.3.2. Static curved surfaces

On the triangulated static sphere, to simulate shape transformation from the spot pattern source ϕ (Fig. 5(a)) to the labyrinth-type pattern target ψ (Fig. 5(f)), we used the values of parameters as $\Delta t = 0.05$, $\epsilon = 3$, and $\alpha = 2$.

In Fig. 5, there are different concentrations of chemicals (phases). In quantitative representation, significantly high chemical concentrations are indicated in red, while comparatively lower chemical concentrations are shown in blue. As the phase transition progresses from chemicals with high concentration to chemicals with low concentration, a complex mixing phenomenon can be observed in Fig. 5(b) and (c). Then, after evolutions as shown in Fig. 5(d) and (e), the interaction of chemicals induces the formation of the labyrinth-type pattern. The transformation of the spot pattern into the new spot–stripe mixed pattern and eventually into the labyrinth-type pattern can be achieved by applying the proposed method on a triangulated spherical surface domain.

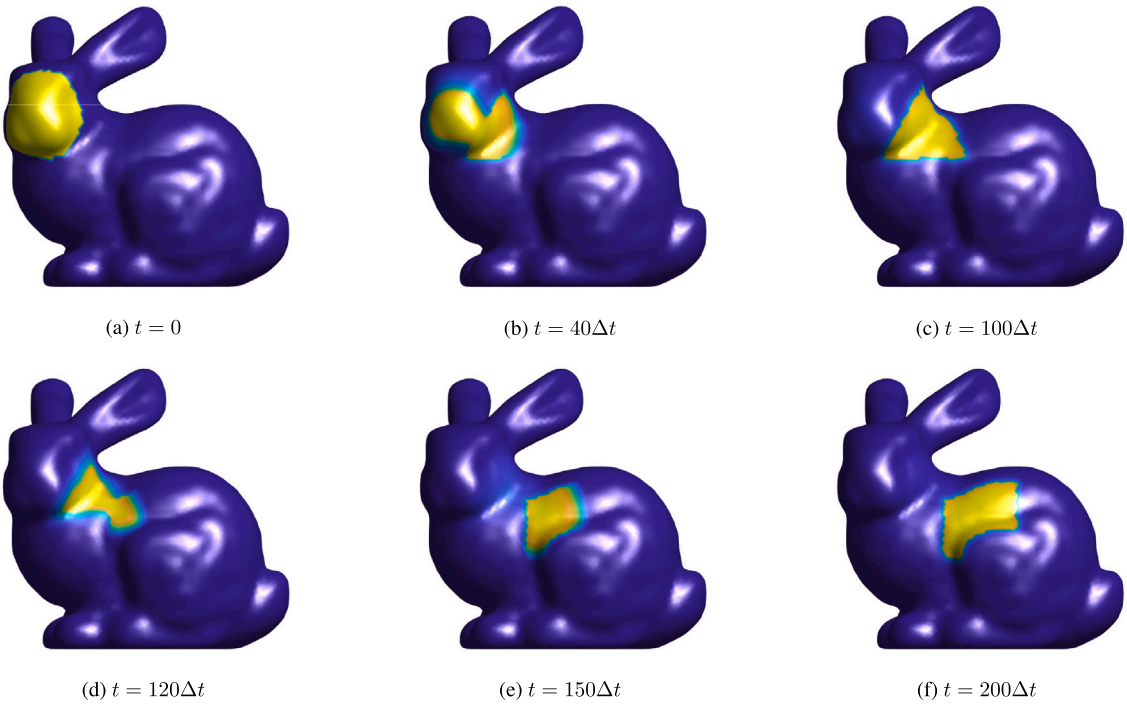

(a) $t = 0$ (b) $t = 40\Delta t$ (c) $t = 100\Delta t$

(d) $t = 120\Delta t$ (e) $t = 150\Delta t$ (f) $t = 200\Delta t$

Fig. 4. (a) circle source shape $\phi(x, y, z, 0)$, the snapshots of shape transformation on Stanford bunny surface in (b)–(f). This shape transformation proceed circle to triangle, and triangle to square.

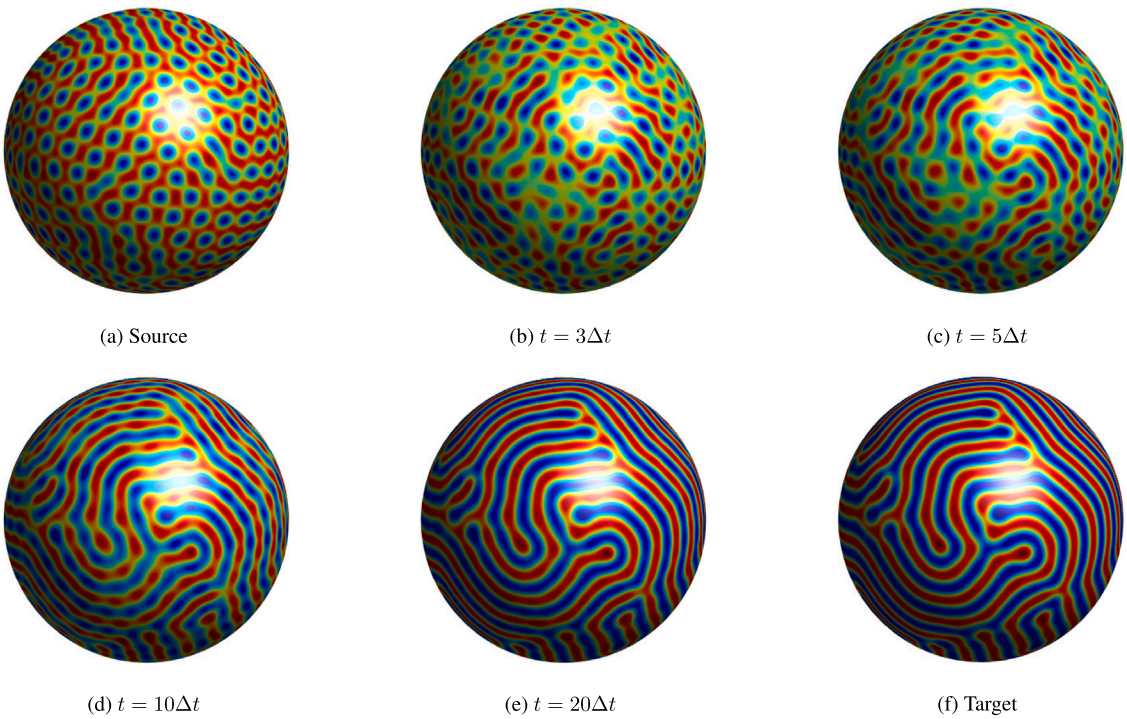

(a) Source (b) $t = 3\Delta t$ (c) $t = 5\Delta t$

(d) $t = 10\Delta t$ (e) $t = 20\Delta t$ (f) Target

Fig. 5. Pattern transformation on the static sphere.

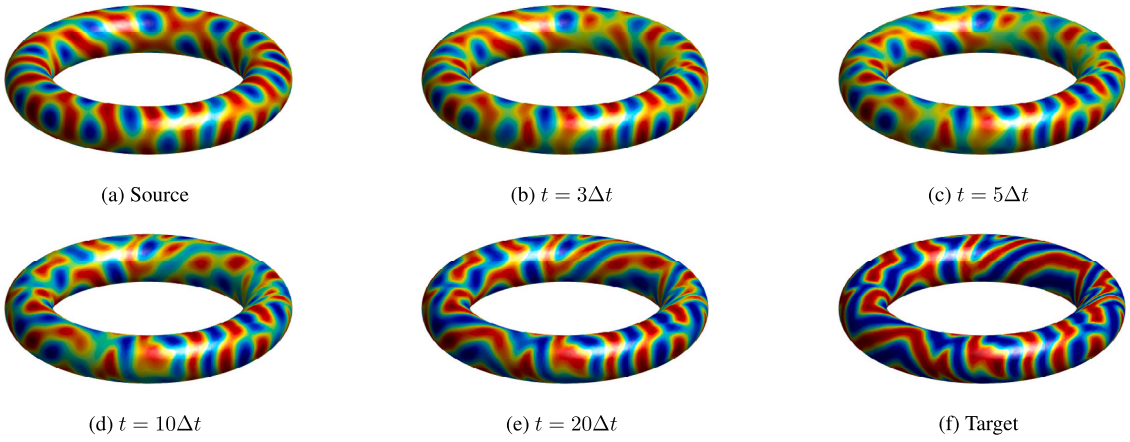

(a) Source (b) $t = 3\Delta t$ (c) $t = 5\Delta t$

(d) $t = 10\Delta t$ (e) $t = 20\Delta t$ (f) Target

Fig. 6. Pattern transformation on the static torus.

To simulate pattern transformation on curved surfaces with different topological structures other than a spherical surface, we consider a triangulated toroidal surface domain. We set the spot pattern source ϕ as shown in Fig. 6(a), and set the labyrinth-type pattern target ψ as shown in Fig. 6(f). The parameter values used are $\Delta t = 0.05$, $\epsilon = 3$, and $\alpha = 2$.

In Fig. 6(b)–(d), the interaction between chemicals occurs within the spot pattern though shape transformation governed by the modified AC equation on the triangulated toroidal surface domain. Phase transition takes place at the interface between high concentration and low concentration phases and results in the transformation of the spot pattern into the spot–stripe mixed pattern along the curvature of the torus. At $t = 20\Delta t$ as shown in Fig. 6(e), it can be seen that the labyrinth-type pattern has been formed when the interaction between the chemicals is almost over.

3.3.3. Evolving curved surfaces

Next, we consider the material evolution on dynamically evolving curved surfaces which is of great significance. As an example, we can investigate the pattern formation [41] on zebra skin during its growth phases. This investigation will be helpful in studying on the complex processes governing the development of patterns on evolving surfaces and give valuable insights into the fundamental understanding of material evolution on surfaces.

On the evolving torus, to implement shape transformation from spot pattern source ϕ to labyrinth-type pattern target ψ, which defined from the reaction–diffusion systems [22,23], we set the parameters as $\Delta t = 0.05$, $\epsilon = 3$ and $\alpha = 1$. Here, surface points on triangulated torus are translated and rotated over time, and shape transformation is performed on this evolving curved surface. This process can be seen in Fig. 7(b)–(e). The initial state torus surface shape as shown in Fig. 7(a) evolves to final state surface shape as shown in Fig. 7(e). At the same time, by the shape transformation, two chemicals in source spot pattern ϕ are interacting to target labyrinth-type pattern ψ on evolving curved surfaces. In the numerical results, we can observe the pattern transformation from spot pattern source (Fig. 7(a)) to labyrinth-type pattern target (Fig. 7(f)) on evolving curved surfaces. Also, it can be observed that the spot pattern is stretched and transformed into stripe shape along curvatures of the evolving curved surface.

Now, to simulate pattern transformation from the labyrinth-type pattern source ϕ to the spot pattern target ψ on the evolving bunny, obtained through the reaction–diffusion systems [22,23], we set the parameters as $\Delta t = 0.002$, $\epsilon = 2$, and $\alpha = 10$. In numerical experiments, we evolve the bunny to twice its initial size, considering the evolving condition as $\mathbf{x}_i(t + \Delta t) = \left(\frac{n\Delta t}{100\Delta t} + 1 \right) \mathbf{x}_i(0)$ where $n = 1, \ldots, 100$ and $\mathbf{x}_i(0)$ is the initial state of the given surface vertices. We then conduct shape transformation on the bunny curved surface using the proposed method. Fig. 8(b)–(e) provide a visual representation of this process. The initial state bunny shape (Fig. 8(a)) evolves to its final state bunny shape (Fig. 8(e)). Simultaneously, using the proposed method, two chemicals in the source labyrinth-type pattern ϕ are involved in transitioning to the target spot pattern ψ on the evolving bunny surface. It can be observed that a pattern in which spots and stripes coexist has been formed in the numerical behavior shown in Fig. 8(b). Subsequently, the stripe-shaped pattern gradually decomposes into spots over time, as depicted in Fig. 8(c)–(d).

3.4. Stable time-stepping scheme

Finally, we present a stable numerical scheme for the proposed mathematical model of shape transformation on curved surfaces. Furthermore, we provide stability analysis and numerical experiments to validate the efficiency of the stable numerical method. We also conduct a comparison test between the fully explicit and stable numerical schemes to demonstrate the superior performance of the stable algorithm. The proposed stable numerical schemes are as follows: First, we apply a semi-implicit method to solve the diffusion equation (5):

$$\frac{\phi_{1,i}^{n+1} - \phi_i^n}{\Delta t} = \Delta_S \phi_i^{n,n+1} = \frac{3}{A(\mathbf{x}_i)} \sum_{j \in V(i)} \frac{\cot \theta_{ij} + \cot \theta_{ij_+}}{2} (\phi_j^n - \phi_{1,i}^{n+1}), \ i = 1, \ldots, N, \tag{19}$$

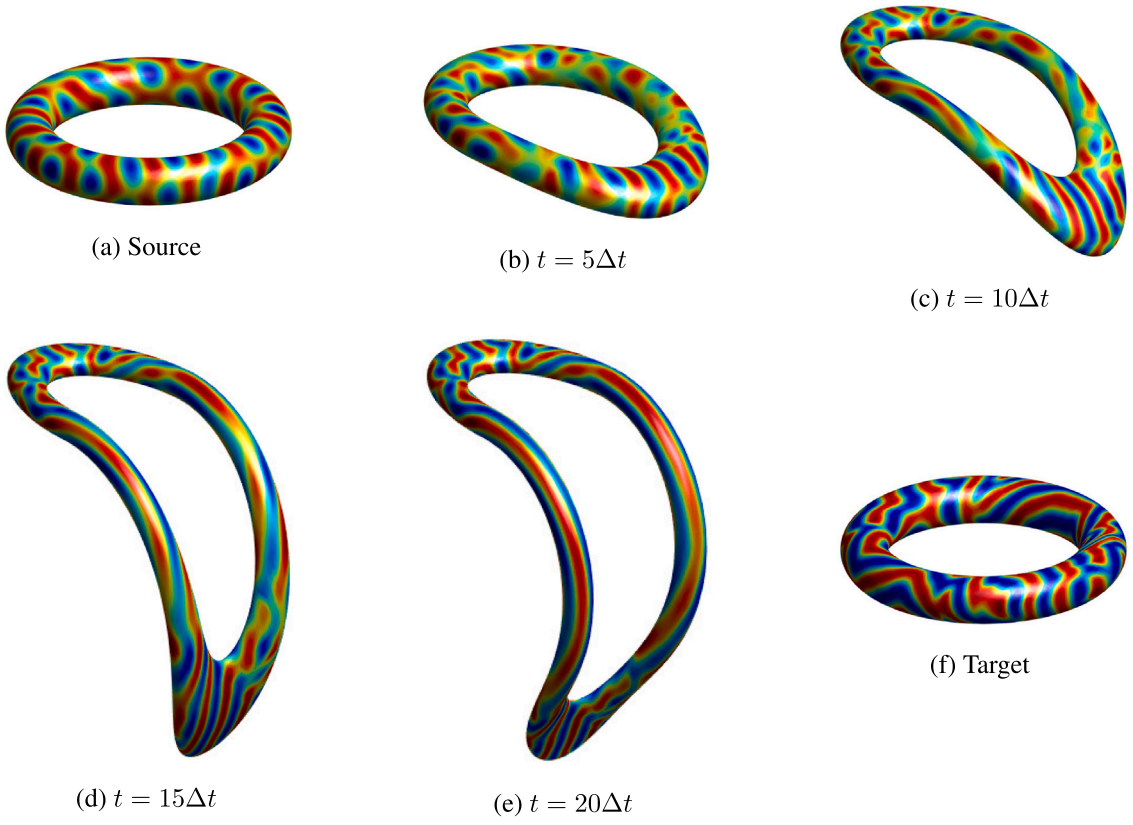

Fig. 7. Pattern transformation on the evolving torus.

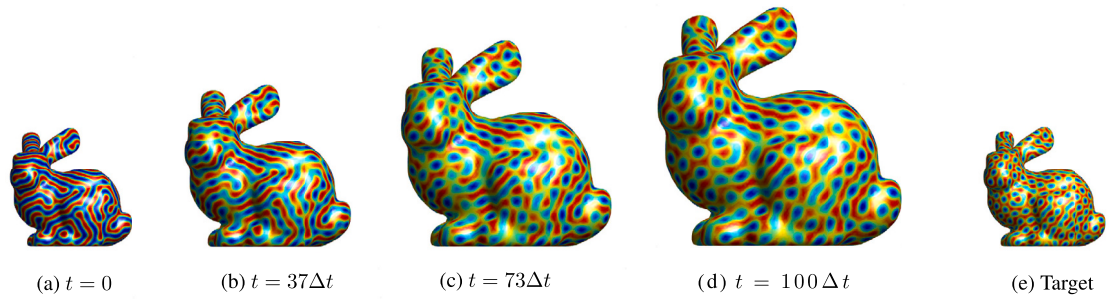

Fig. 8. Pattern transformation on the evolving (a) original size bunny to (d) double size bunny.

which can be rewritten as

$$\phi_{1,i}^{n+1} = \left(\phi_i^n + \frac{3\Delta t}{A(\mathbf{x}_i)} \sum_{j \in V(i)} \frac{\cot\theta_{ij} + \cot\theta_{ij_+}}{2} \phi_j^n \right) \Bigg/ \left(1 + \frac{3\Delta t}{A(\mathbf{x}_i)} \sum_{j \in V(i)} \frac{\cot\theta_{ij} + \cot\theta_{ij_+}}{2} \right). \tag{20}$$

Here, we applied the unconditionally positive FDM [42] to efficiently and stably solve the diffusion equation on triangular meshes on curved surfaces.

Next, the other two solutions for Eqs. (6) and (7) are identical to the first scheme, i.e.,

$$\phi_{2,i}^{n+1} = \frac{\phi_{1,i}^{n+1}}{\sqrt{\left(1 - \left(\phi_{1,i}^{n+1}\right)^2\right) e^{-\frac{2\Delta t}{\epsilon^2}} + \left(\phi_{1,i}^{n+1}\right)^2}}. \tag{21}$$

and

$$\phi_i^{n+1} = \phi_{3,i}^{n+1} = \frac{\phi_{2,i}^{n+1} + \Delta t\alpha\psi_i\sqrt{F\left(\phi_{2,i}^{n+1}\right)}}{1 + \Delta t\alpha\sqrt{F\left(\phi_{2,i}^{n+1}\right)}}. \tag{22}$$

3.4.1. Stability analysis of the stable time-stepping scheme

Now, we consider the stability analysis for the proposed stable numerical schemes. Let us assume $\|\phi_1^n\|_\infty \le 1$ and all triangular surface meshes are acute triangles. Then, from Eq. (20), we have

$$|\phi_{1,i}^{n+1}| \le \left(|\phi_i^n| + \frac{3\Delta t}{A(\mathbf{x}_i)}\sum_{j\in V(i)}\frac{\cot\theta_{ij} + \cot\theta_{ij_+}}{2}|\phi_j^n|\right) \Bigg/ \left(1 + \frac{3\Delta t}{A(\mathbf{x}_i)}\sum_{j\in V(i)}\frac{\cot\theta_{ij} + \cot\theta_{ij_+}}{2}\right) \tag{23}$$

$$\le 1,\ i = 1,\dots,N, \tag{24}$$

where we have used $0 < \theta_{ij} < \pi/2$ and $0 < \theta_{ij_+} < \pi/2$, i.e., $\cot\theta_{ij} > 0$ and $\cot\theta_{ij_+} > 0$. Therefore, $\|\phi_1^{n+1}\|_\infty \le 1$ holds for any Δt. Next, from Eq. (21), we have

$$|\phi_{2,i}^{n+1}| = \frac{|\phi_{1,i}^{n+1}|}{\sqrt{\left(1 - \left(\phi_{1,i}^{n+1}\right)^2\right)e^{-\frac{2\Delta t}{\epsilon^2}} + \left(\phi_{1,i}^{n+1}\right)^2}} \le 1,\ i = 1,\dots,N, \tag{25}$$

where we have used $1 - \left(\phi_{1,i}^{n+1}\right)^2 \ge 0$ because of $\|\phi_1^{n+1}\|_\infty \le 1$. Therefore, $\|\phi_2^{n+1}\|_\infty \le 1$ holds for any Δt. Finally, from Eq. (22), we have

$$|\phi_i^{n+1}| \le \frac{|\phi_{2,i}^{n+1}| + \Delta t\alpha|\psi_i|\sqrt{F\left(\phi_{2,i}^{n+1}\right)}}{1 + \Delta t\alpha\sqrt{F\left(\phi_{2,i}^{n+1}\right)}} \le 1,\ i = 1,\dots,N, \tag{26}$$

where we have used $\|\phi_2^{n+1}\|_\infty \le 1$ and $\|\psi\|_\infty \le 1$. Hence, $\|\phi^{n+1}\|_\infty \le 1$ holds for any Δt and the proposed numerical scheme (20)–(22) is unconditionally stable.

3.4.2. Comparison test between fully explicit and stable time-stepping schemes

In this section, we shall perform comparative numerical experiments between the fully explicit time-stepping scheme, described in Section 2.2, and a stable time-stepping scheme outlined in Section 3.4. To compare the numerical behaviors of the fully explicit and stable time-stepping schemes, we use a source and target of simple shapes on basic curved surfaces as shown in Fig. 2. In this test, all parameter values are the same, except for the time step size Δt and the interfacial thickness ϵ. Different values of ϵ are applied because, with an increase in the time step size, a small value of ϵ leads to the pinning effect and hinders the shape transformation. We use the parameter values as $\Delta t = 0.05$, $\epsilon = 3$, and $\alpha = 10$ for the fully explicit time-stepping scheme. For the stable time-stepping scheme, the parameter values are set as $\Delta t = 1$, $\epsilon = 10$, and $\alpha = 10$.

In Fig. 9, the numerical behaviors for the proposed schemes are presented. Fig. 9(a)–(e) display the shape transformation from a circle to a square on the spherical surface using the fully explicit time-stepping scheme. Fig. 9(f)–(j) present the shape transformation from a circle to a square on the spherical surface using the stable time-stepping scheme. From the observed numerical behaviors, it is evident that the evolutionary speed is approximately twice as fast when the stable scheme is applied. Despite the time step size differing by a factor of 20, the evolutionary speed appears to differ by about 2 times because there is a natural discretion error associated with the larger time step.

4. Discussions

The shape transformation on evolving curved surfaces is an important research topic for the following reasons: In biological applications, this approach can offer valuable insight into studying the morphological transformation of evolving biological surfaces such as the growth of organs or tissues; and it can also provide understanding on how cells or organic shapes can be manipulated over time, thereby facilitating the discovery of the fundamental principles that govern these transformations. Furthermore, in materials science and engineering, this approach can be applied to investigate the shape deformation of materials on curved surfaces, particularly within the domains of manufacturing and designing smart materials. It helps exploration into how the curvature of surfaces influences the mechanical properties and shape memory effects of materials. Moreover, this approach can also be considered when examining how the shape of natural surfaces evolves in response to environmental factors over time. Studying such changes has implications for ecosystem monitoring.

In the future work, we shall numerically study data assimilation for physical phenomena in fluid dynamics systems on curved surfaces, using the proposed modified surface AC type equation. In addition, we shall study to solve the system by coupling the incompressible Navier–Stokes equation with the proposed modified surface AC model. This approach will enable the numerical

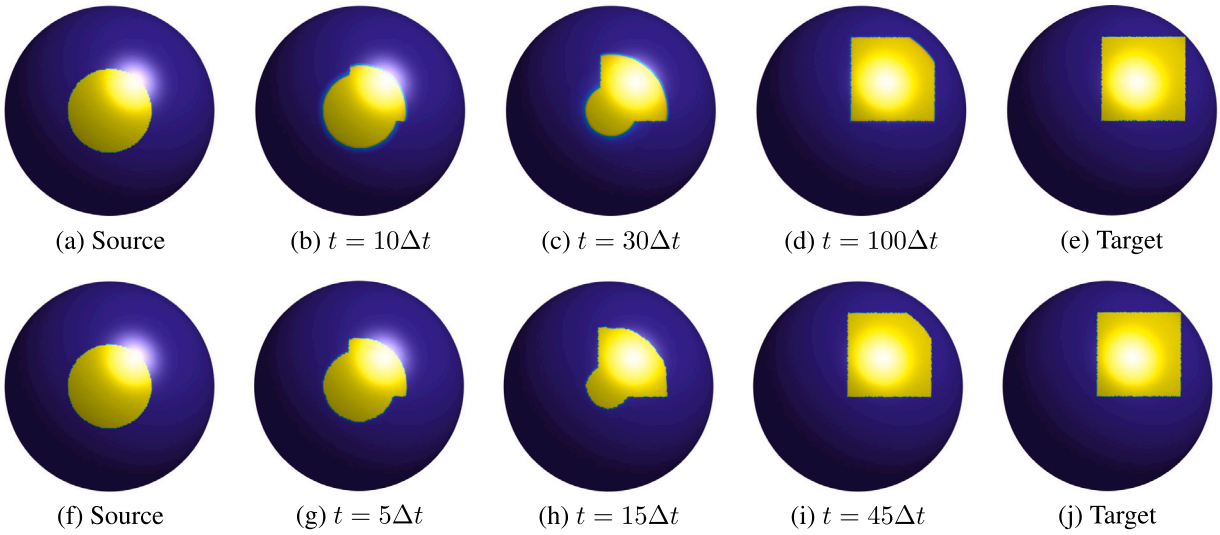

Fig. 9. Shape transformations using the (a)–(e): existing explicit time-stepping scheme, and (f)–(j): stable time-stepping scheme.

implementation and simulation of two representative phenomena: the occurrence of a tsunami when a fault is shifted on the seafloor of the Earth's surface; and the process of sediment accumulation on a fault under fluid flow conditions, using the multi-phase modified surface AC model. Furthermore, we shall investigate how shape transformations impact the aerodynamics or hydrodynamics of surfaces in motion, using the multi-phase modified surface AC system with a non-standard variable mobility.

5. Conclusions

In this work, we presented the shape transformation on curved surfaces using the modified surface AC equation with the fidelity term. The numerical solution algorithms of the modified surface AC equation with fidelity term consist of the three subproblems by operator splitting method, that is, the diffusion term, reaction term and fidelity term. The diffusion term is solved by the explicit Euler method and simple discretization of the Laplace–Beltrami operator. The separation of variable is used to solve the reaction term, and semi-implicit Euler method utilizes to solve the fidelity term. Next, we performed numerical experiments to demonstrate the shape transformation on curved surfaces. In the numerical results, we observed that the shape and image transformation performed on simple and complex surfaces using the proposed method. In addition, we further extended our approach by developing an unconditionally stable scheme on the curved surfaces. The numerical experiments demonstrated the proposed unconditionally stable scheme is efficient and robust for simulating the shape transformations on curved surfaces. For future works, we will focus on developing second-order schemes [43] to enhance the accuracy and efficiency of the simulations. Additionally, we plan to explore more advanced numerical methods [44] and investigate their applicability to a wider range of problems in shape transformation on curved surfaces.

CRediT authorship contribution statement

Hyundong Kim: Writing – review & editing, Writing – original draft, Visualization, Validation, Supervision, Software, Resources, Project administration, Methodology, Investigation, Formal analysis, Data curation, Conceptualization. **Seungyoon Kang:** Writing – review & editing, Writing – original draft, Visualization, Validation, Investigation. **Gyeonggyu Lee:** Writing – original draft, Visualization, Validation, Investigation. **Sungha Yoon:** Writing – review & editing, Formal analysis, Investigation, Visualization, Resources. **Junseok Kim:** Writing – review & editing, Writing – original draft, Supervision, Software, Project administration, Methodology, Investigation, Funding acquisition, Formal analysis, Conceptualization.

Declaration of competing interest

The authors declare that they have no known competing financial interests or personal relationships that could have appeared to influence the work reported in this paper.

Data availability

Data will be made available on request.

Acknowledgments

The first author (Hyundong Kim) was supported by Basic Science Research Program through the National Research Foundation of Korea (NRF) funded by the Ministry of Education, Republic of Korea (NRF-2020R1A6A3A13077105). Sungha Yoon was supported by the National Research Foundation of Korea (NRF) grant funded by the Ministry of Science and ICT of Korea (MSIT) (No. 2019R1A6A1A11051177) and by Basic Science Research Program through the National Research Foundation of Korea (NRF) funded by the Ministry of Education (MOE) (No. 2022R1I1A1A01073661). The corresponding author (J.S. Kim) was supported by the National Research Foundation of Korea (NRF) grant funded by the Korea government (MSIT) (No. 2022R1A2C1003844). The authors are grateful to the reviewers for valuable comments on the revision of this article.

References

[1] Specht M, Lebrun R, Zollikofer CP. Visualizing shape transformation between chimpanzee and human braincases. Vis Comput 2007;23:743–51.
[2] Yazdani A, Bagchi P. Three-dimensional numerical simulation of vesicle dynamics using a front-tracking method. Phys Rev E 2012;85:056308.
[3] Lee H, Seo YJ, Kim J, Bae MJ, Hwang S, Bae JG, Lee WB, Yoon H. Function transformation of polymeric films through morphing of surface shapes. Chem Eng J 2022;434:134665.
[4] Wang Y, Hu D, Chang X, Zhu Y. Temperature-driven reversible shape transformation of polymeric nanoparticles from emulsion confined coassembly of block copolymers and poly (N-isopropylacrylamide). Macromolecules 2022;55:6211–9.
[5] Li Y, Song X, Kwak S, Kim J. Weighted 3D volume reconstruction from series of slice data using a modified Allen–Cahn equation. Pattern Recognit 2022;132:108914.
[6] Kim H, Lee C, Kwak S, Hwang Y, Kim S, Choi Y, Kim J. Three-dimensional volume reconstruction from multi-slice data using a shape transformation. Comput Math Appl 2022;113:52–8.
[7] Allen SM, Cahn JW. A microscopic theory for antiphase boundary motion and its application to antiphase domain coarsening. Acta Mater 1979;27:1085–95.
[8] Lee C, Kim H, Yoon S, Kim S, Lee D, Park J, Kwak S, Yang J, Wang J, Kim J. An unconditionally stable scheme for the Allen–Cahn equation with high-order polynomial free energy. Commun Nonlinear Sci Numer Simul 2021;95:105658.
[9] Jeong D, Li Y, Lee H, Lee S, Yang J, Park S, Kim H, Choi Y, Kim J. Efficient 3D volume reconstruction from a point cloud using a phase-field method. Math Probl Eng 2018;2018.
[10] Li Y, Jeong D, Choi JI, Lee S, Kim J. Fast local image inpainting based on the Allen–Cahn model. Digit Signal Process 2015;37:65–74.
[11] Budd J, Gennip Yvan, Latz J. Classification and image processing with a semi-discrete scheme for fidelity forced Allen–Cahn on graphs. GAMM-Mitt 2021;44:e202100004.
[12] Wang J, Li Y, Choi Y, Lee C, Kim J. Fast and accurate smoothing method using a modified Allen–Cahn equation. Comput Aided Des 2020;120:102804.
[13] Li Y, Wang K, Yu Q, Xia Q, Kim J. Unconditionally energy stable schemes for fluid-based topology optimization. Commun Nonlinear Sci Numer Simul 2022;111:106433.
[14] Li Y, Kim J. An unconditionally stable hybrid method for image segmentation. Appl Numer Math 2014;82:32–43.
[15] Xia B, Li Y, Li Z. Second-order unconditionally stable direct methods for Allen–Cahn and conservative Allen–Cahn equations on surfaces. Mathematics 2020;8:1486.
[16] Choi Y, Li Y, Lee C, Kim H, Kim J. Explicit hybrid numerical method for the Allen–Cahn type equations on curved surfaces. Numer Math Theor Meth Appl 2021;14:797–810.
[17] Kim H, Yoon S, Wang J, Lee C, Kim S, Park J, Kim J. Shape transformation using the modified Allen–Cahn equation. Appl Math Lett 2020;107:106487.
[18] Wang Y, Xiao X, Feng X. An efficient maximum bound principle preserving p-adaptive operator-splitting method for three-dimensional phase field shape transformation model. Comput Math Appl 2022;120:78–91.
[19] Saul'ev VKE. A method of numerical integration of diffusion equations. Doklady Akademii Nauk 1957;115:1077–9.
[20] Campbell LJ, Yin B. On the stability of alternating-direction explicit methods for advection-diffusion equations. Numer Methods Part Differ Equ 2007;23:1429–44.
[21] Kim H, Lee C, Yoon S, Choi Y, Kim J. A fast shape transformation using a phase-field model. Extreme Mech Lett 2022;52:101633.
[22] Kim H, Yun A, Yoon S, Lee C, Park J, Kim J. Pattern formation in reaction–diffusion systems on evolving surfaces. Comput Math Appl 2020;80:2019–28.
[23] Kim H. Explicit time-stepping approach for pattern formation on evolving curved surfaces. Ph. D. dissertation, Korea University; 2022.
[24] Xu G. Discrete Laplace–Beltrami operators and their convergence. Comput Aided Geom Design 2004;21:767–84.
[25] Xu G. Convergence of discrete Laplace–Beltrami operators over surfaces. Comput Math Appl 2004;48:347–60.
[26] Desbrun M, Meyer M, Schröder P, Barr AH. Implicit fairing of irregular meshes using diffusion and curvature flow. In: SIGGRApH '99: proceedings of the 26th annual conference on computer graphics and interactive techniques. 1999, p. 317–24.
[27] Meyer M, Desbrun M, Schröder P, Barr AH. Discrete differential-geometry operators for triangulated 2-manifolds. Vis Math 2003;3:35–57.
[28] Gotsman C, Gu X, Sheffer A. Fundamentals of spherical parameterization for 3D meshes. In: ACM SIGGRApH 2003 papers. 2003, p. 358–63.
[29] Fathi H, Ahmadyfard AR, Khosravi H. Deformable 3D shape matching to try on virtual clothes via Laplacian–Beltrami descriptor. J AI Data Min 2022;10:63–74.
[30] Xia Q, Yu Q, Li Y. A second-order accurate, unconditionally energy stable numerical scheme for binary fluid flows on arbitrarily curved surfaces. Comput Meth Appl Mech Eng 2021;384:113987.
[31] Li Y, Liu R, Xia Q, He C, Li Z. First-and second-order unconditionally stable direct discretization methods for multi-component Cahn–Hilliard system on surfaces. J Comput Appl Math 2022;401:113778.
[32] Yang J, Kim J. An unconditionally stable second-order accurate method for systems of Cahn–Hilliard equations. Commun Nonlinear Sci Numer Simul 2020;87:105276.
[33] Yang J, Kim J. Numerical study of the ternary Cahn–Hilliard fluids by using an efficient modified scalar auxiliary variable approach. Commun Nonlinear Sci Numer Simul 2021;102:105923.
[34] Lin F, He X, Wen X. Fast, unconditionally energy stable large time stepping method for a new Allen–Cahn type square phase-field crystal model. Appl Math Lett 2019;98:248–55.
[35] Xu G. Convergent discrete Laplace–Beltrami operators over triangular surfaces. GMP 2004;195–204.
[36] Zhang C, Wang H, Huang J, Wang C, Yue X. A second order operator splitting numerical scheme for the good Boussinesq equation. Appl Numer Math 2017;119:179–93.
[37] Liu C, Wang C, Wang Y. A second-order accurate, operator splitting scheme for reaction–diffusion systems in an energetic variational formulation. SIAM J Sci Comput 2022;44:A2276–301.
[38] Liu C, Wang C, Wang Y. A structure-preserving, operator splitting scheme for reaction–diffusion equations with detailed balance. J Comput Phys 2021;436:110253.

[39] Liu C, Wang C, Wang Y, Wise SM. Convergence analysis of the variational operator splitting scheme for a reaction–diffusion system with detailed balance. SIAM J Numer Anal 2022;60:781–803.
[40] Li Y, Kim J, Wang N. An unconditionally energy-stable second-order time-accurate scheme for the Cahn-Hilliard equation on surfaces. Commun Nonlinear Sci Numer Simul 2017;53:213–27.
[41] Yang J, Kim J. Computer simulation of the nonhomogeneous zebra pattern formation using a mathematical model with space-dependent parameters. Chaos Solitons Fractals 2023;169:113249.
[42] Jalghaf HK, Kovács E, Majár J, Á Nagy, Askar AH. Explicit stable finite difference methods for diffusion-reaction type equations. Mathematics 2021;9:3308.
[43] Yang J, Kim J. An unconditionally stable second-order accurate method for systems of Cahn–Hilliard equations. Commun Nonlinear Sci Numer Simul 2020;87:105276.
[44] Cheng J, Xia Q, Kim J, Li Y. An efficient linear and unconditionally stable numerical scheme for the phase field sintering model. Commun Nonlinear Sci Numer Simul 2023;127:107529.